Frontiers of Physics
https://doi.org/10.1007/s11467-018-0870-3

Front. Phys.
14(2), 23502 (2019)

LETTER

Physical properties of quaternary compounds $Gd_2CoAl_4T_2$ (T = Si, Ge) single crystals

Kaijian Huang[1], **Yuanshuai Sun**[2], **Shanshan Sun**[2], **Xiao Zhang**[3,†], **Hechang Lei**[2,‡]

[1] *College of Civil Engineering, Nanjing Forestry University, Nanjing 210037, China*
[2] *Department of Physics and Beijing Key Laboratory of Opto-electronic Functional Materials & Micro-nano Devices, Renmin University of China, Beijing 100872, China*
[3] *State Key Laboratory of Information Photonics and Optical Communications & School of Science, Beijing University of Posts and Telecommunications, Beijing 100876, China*
Corresponding authors. E-mail: † *zhangxiaobupt@bupt.edu.cn,* ‡ *hlei@ruc.edu.cn*

Received October 2, 2018; accepted October 22, 2018

We have synthesized and investigated physical properties of two new quaternary compounds $Gd_2CoAl_4T_2$ (T = Si, Ge) single crystals, which are isostructural to $Tb_2NiAl_4Ge_2$ and $Er_2CoAl_4Ge_2$. The most important structural feature of these materials is the anti-CaF_2-type $CoAl_4T_2$ slabs. These materials show metallic behavior below 300 K and there is a long-range antiferromagnetic (AFM) transition appearing at 20 and 27 K for $Gd_2CoAl_4Ge_2$ and $Gd_2CoAl_4Si_2$, respectively. Resistivity and heat capacity measurements also confirm these bulk AFM transitions. Further analysis indicates that this long-range antiferromagnetism should result from the magnetic interaction between local moments of Gd^{3+} ions.

Keywords magnetic materials, rare earth compounds, single crystal growth

1 Introduction

High-temperature metal solutions as flux are indispensable methods to grow single crystals with diverse exotic physical properties [1, 2]. Among a variety of metal flux, Al flux has some unique features. For example, it can dissolve a large number of elements, especially boron. Thus, Al flux is an important method to grow metal borides single crystals, such as transition metal and rare earth borides [3, 4]. Furthermore, Al can be dissolved readily not only in nonoxidizing acids but also in bases. This property is very important to synthesis single crystals that are easy to decompose in acids but not in bases. In addition, Al flux can also be used as a reaction flux to grow complex (ternary or quaternary) aluminides, especially alumosilicides and alumogermanides, because the phase diagrams of the Al-Si and Al-Ge show low eutectic points without forming any binary phases. A large amount of intermetallic alumosilicides and alumogermanides have been prepared from liquid Al, such as $RENiAl_4Ge_2$ (RE = Sm, Tb, Y) [5], $Sm_2Ni(Ni, Si)Al_4Si_6$ [6], and $RE_8Ru_{12}Al_{49}Si_9(Al_xSi_{12-x})$ (RE = Sm, Pr) etc [7].

In this work, we discovered two new quaternary compounds $Gd_2CoAl_4T_2$ (T = Si, Ge) using Al flux. They are isostructural to $Tb_2NiAl_4Ge_2$ and $Er_2CoAl_4Ge_2$ [8, 9]. Detailed study on physical properties shows that these materials are metals with long-range antiferromagnetic (AFM) transition at low temperature. These AFM orderings can be mainly ascribed to the magnetic interaction of local moments of Gd^{3+} ions.

2 Experiment

$Gd_2CoAl_4T_2$ (T = Si, Ge) single crystals were grown by the Al flux method. Gd chunks (99.99%), Co lumps (99.99%), Al grains (99.99%) and Si or Ge granular (99.9999%) were mixed together in a molar ratio of Gd : Co : Al : T = 2 : 1 : 2 : 18 and placed in an alumina crucible. Then, the crucible was sealed in the quartz ampoule under partial argon atmosphere. The sealed quartz ampoule was heated up to 1323 K for 12 h and then kept at that temperature for 4 h. Finally the ampoule was cooled down slowly to 1023 K with 5 K/h. At this temperature, the ampoule was decanted with a centrifuge to extract single crystals from the Al flux. X-ray diffraction (XRD) patterns were collected using a Bruker D8 X-ray diffractometer with Cu K_α radiation ($\lambda = 0.15418$ nm) at room temperature. The elemental analysis was performed using energy-dispersive X-ray spectroscopy (EDX) analyses. Electrical transport measurements were carried out in a Quantum Design physical property measurement system (PPMS-14). The electrical resistivity was measured using a four-probe method on rectangular-shaped single crystals. The current flows in the *ab* plane of the crystal. Magnetization measurements were performed in a Quantum Design magnetic property measurement system (MPMS3).

3 Results and discussion

Figure 1(a) shows the powder XRD pattern of ground $Gd_2CoAl_4Ge_2$ single crystals. It can be fitted well by using the structure of $Er_2CoAl_4Ge_2$ with the space group I4/mmm (No. 139). The fitted a- and c-axial lattice parameters are 4.1392(3) Å and 19.543(2) Å for $Gd_2CoAl_4Ge_2$ (also shown in Table 1), which are larger than those in $Er_2CoAl_4Ge_2$ (a = 4.0971 Å and c = 19.331 Å) [9]. It can be ascribed to the larger ionic radius of Gd than Er. On the other hand, when exploring the Gd-Co-Al-Si system we found that the powder XRD pattern of ground single crystals can also be fitted using above structure. The obtained lattice parameters from fitting give a = 4.1099(1) Å and c = 19.4146(8) Å for $Gd_2CoAl_4Si_2$, which are smaller than those in $Gd_2CoAl_4Ge_2$, because of smaller ionic radius of Si when compared to Ge. Correspondingly, the volume of unit cell V for $Gd_2CoAl_4Si_2$ is also smaller than that for $Gd_2CoAl_4Ge_2$ (Table 1). The composition analysis further confirms the formation of $Gd_2CoAl_4Si_2$. The atomic ratio of Gd : Co : Al : Si determined from the EDX measurement is 2 : 1.02 : 3.82 : 2.09 when setting Gd as 2, close to the chemical formula of $Gd_2CoAl_4Si_2$. Figures 1(c) and (d) show the XRD patterns of $Gd_2CoAl_4T_2$ single crystals. There are only the $(00l)$ diffraction peaks appearing, indicating that the crystal surface is parallel to the ab-plane and the diffraction peaks of $Gd_2CoAl_4Ge_2$ shift to lower angles compared to the $Gd_2CoAl_4Si_2$ single crystal, consistent with the larger c axial lattice parameter of the former. The thick plate-like shapes of crystals [insets of Figs. 1(c) and (d)] are consistent with the crystal orientation and the layered structure of $Gd_2CoAl_4T_2$ mentioned below.

As shown in Fig. 2(a), the structure of $Gd_2CoAl_4T_2$ is built up by stacking $CoAl_4T_2$ slabs and bilayer of Gd atoms alternatively along the c axis. Similar to the $NiAl_4Ge_2$ unit in $Tb_2NiAl_4Ge_2$ [8], the $CoAl_4T_2$ slab has an antiflourite (anti-CaF_2) structure type, where T and Co occupy the site of Ca and F is replaced by Al. Thus, each Al atom is coordinated by two T and two Ni atoms, forming a tetrahedron. Two layers of these $AlCo_2T_2$ tetrahedra connect each other via edge sharing and form a two-dimensional $[CoAl_4T_2]^{\infty}_{2D}$ slab [Fig. 2(b)]. On the other

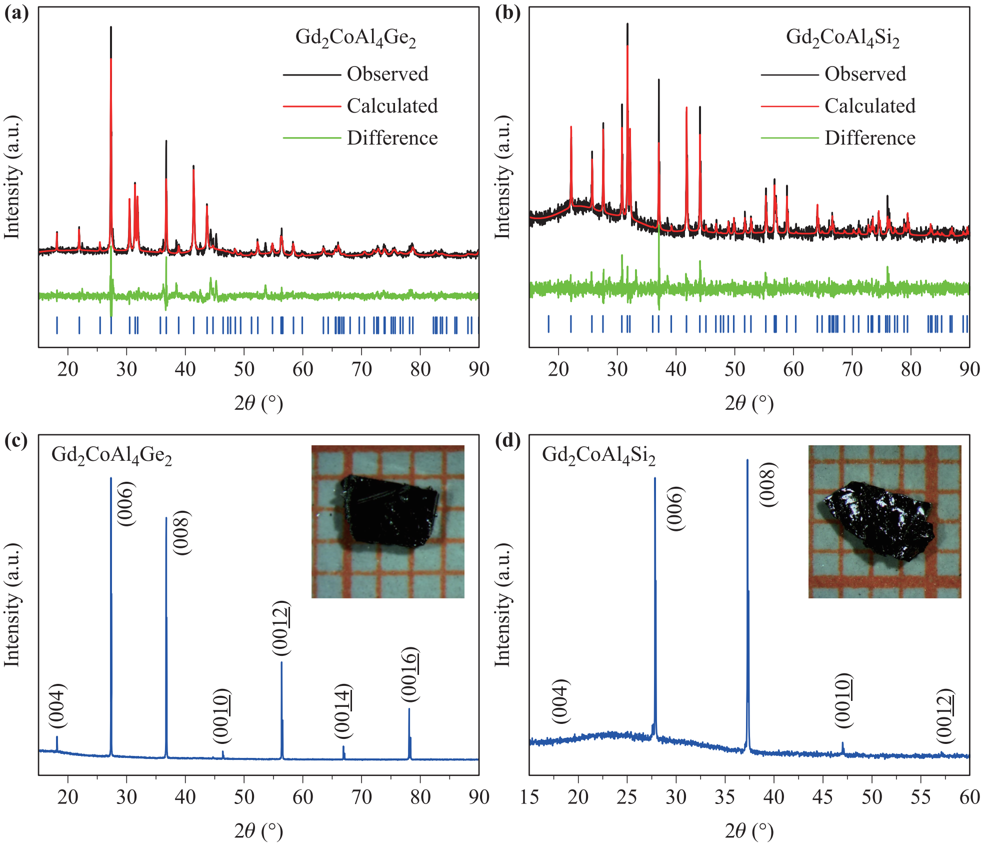

Fig. 1 **(a, b)** Powder XRD patterns and refinements of ground $Gd_2CoAl_4T_2$ single crystals. **(c, d)** XRD patterns of $Gd_2CoAl_4T_2$ single crystals. Insets of (c) and (d): Photograph of $Gd_2CoAl_4T_2$ single crystals. The length of one grid in the photograph is 1 mm.

Table 1 Lattice parameters, atomic positions, and selected bond lengths of $Gd_2CoAl_4T_2$ (T = Si, Ge).

Chemical formula	$Gd_2CoAl_4Si_2$	$Gd_2CoAl_4Ge_2$
Space group	I4/mmm	I4/mmm
a (Å)	4.1099(1)	4.1392(3)
c (Å)	19.4146(8)	19.543(2)
V (Å^3)	327.94(3)	334.84(5)

Atom	Wyckoff	x	y	z (Si)	z (Ge)
Gd	4e	0	0	0.1861(3)	0.1837(3)
Co	2a	0	0	0	0
Al	8g	0	0.5	0.069(1)	0.0599(8)
T	4e	0	0	0.333(1)	0.3381(6)

Bond length d (Å)	$Gd_2CoAl_4Si_2$	$Gd_2CoAl_4Ge_2$
Gd-Gd	3.822(7)	3.909(8)
Si/Ge-Al	2.80(2)	2.87(1)
Co-Al	2.45(1)	2.378(8)
Al-Al (in ab plane)	2.9061(1)	2.9269(2)
Al-Al (out of ab plane)	2.67(4)	2.34(3)

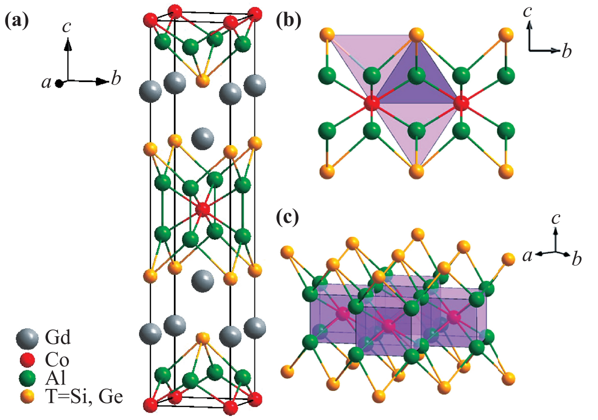

Fig. 2 **(a)** Crystal structure of $Gd_2CoAl_4T_2$. Enlarged view of $CoAl_4T_2$ slab when highlighting the connection of **(b)** distorted $AlCo_2T_2$ tetrahedra and **(c)** distorted $CoAl_8$ cubes.

hand, the local structure of $CoAl_4T_2$ slab can also be described as following [8]. Each Co atom is surrounded by eight Al atoms, consisting of a slightly distorted $CoAl_8$ cube. These distorted $CoAl_8$ cubes connect each other by edge sharing and form an infinite layer with one half of the cubes filled with a Co center. The T atoms then are located above and below the Al_8 cubes which are not centered by Co atoms [Fig. 2(c)]. The fitted atomic positions for Gd, Co, Al and T are shown in Table 1. The values are close to those in $Tb_2NiAl_4Ge_2$ and $Er_2CoAl_4Ge_2$ [8, 9]. As shown in Table 1, the $d_{\mathrm{Gd-Gd}}$, $d_{\mathrm{Si/Ge-Al}}$ and $d_{\mathrm{Al-Al}}$ (in the ab plane) for $Gd_2CoAl_4Si_2$ are slightly smaller than those for $Gd_2CoAl_4Ge_2$, which can be ascribed to the smaller lattice parameters of the former. But the $d_{\mathrm{Co-Al}}$ and $d_{\mathrm{Al-Al}}$ (out of ab plane) for the former are abnormally larger than those for the latter. It suggests that the distorted $CoAl_8$ cubes in $Gd_2CoAl_4Si_2$ expand along the c axis and one of possible explanation is that the stronger bonding strength of Si-Al weakens those of Co-Al and Al-Al because of larger electronegativity of Si than Ge.

Figure 3(a) shows the temperature dependence of magnetic susceptibility $\chi(T)$ of the $Gd_2CoAl_4Ge_2$ single crystal at $H = 1$ kOe along the ab plane and the c axis with zero-field-cooling (ZFC) and field-cooling (FC) modes. There are sharp drops below 20 K in both ZFC and FC curves, and it can be ascribed to the onset of long-range AFM ordering. The Weiss temperature T_N determined from the peak of $\mathrm{d}(\chi T)/\mathrm{d}T(T)$ curves with ZFC mode is 20.1 and 20.0 K for $H//ab$ and $H//c$ [inset of Fig. 3(a)] [10]. These values are close to that in $Tb_2NiAl_4Ge_2$ [8]. The decrease of $\chi_{ab}(T)$ below T_N is more obvious than $\chi_c(T)$, strongly suggesting that the spin is ordered antiferromagnetically in the ab-plane (easy plane of magnetization). When $T > T_N$, the $\chi(T)$ decrease with increasing temperature for both field directions and they can be fitted very well using the Curie–Weiss (CW) law $\chi(T) = C/(T - \theta)$, where C is Curie constant and θ is the CW temperature. The linear fits for the curves of $1/\chi(T)$ vs. T between 50 and 300 K with ZFC mode (solid lines in Fig. 3(c)) give $C = 0.027110(6)$ emu·g^{-1}·Oe^{-1}·K and $\theta = -30.93(5)$ K for $H//ab$, and $C = 0.029280(8)$ emu·g^{-1}·Oe^{-1}·K and $\theta = -34.24(6)$ K for $H//c$. The negative values of θ indicate the AFM interaction in this material, consistent with the AFM ordering below T_N. The values of C correspond to the effective moment $\mu_{\mathrm{eff}} = 8.2433(9)$ and $8.567(1)$ μ_{B}/Gd for $H//ab$ and $H//c$. These values are close to the theoretical value of free Gd^{3+} ion (7.94 μ_{B}/Gd). It suggests that Co ions may not have local moments in $Gd_2CoAl_4Ge_2$ as in the case in $Tb_2NiAl_4Ge_2$ and other rare earth-cobalt-aluminum compounds [8, 11]. For $Gd_2CoAl_4Si_2$, there is also a drop in the $\chi(T)$ curve at low temperature [Fig. 3(b)], corresponding to the AFM transition. The determined T_N from the peak of $\mathrm{d}(\chi T)/\mathrm{d}T(T)$ curves is 26.4 and 26.8 K for $H//ab$ and $H//c$ [inset of Fig. 3(b)], slightly higher than those in $Gd_2CoAl_4Ge_2$. It could be due to the smaller $d_{\mathrm{Gd-Gd}}$ in the former. The easy plane of magnetization in $Gd_2CoAl_4Si_2$ is also the ab-plane because of the faster drop of $\chi_{ab}(T)$ than $\chi_c(T)$. From the linear fits of $1/\chi(T)$ curves [solid lines in Fig. 3(c)], the obtained C and θ are 0.031690(7) emu·g^{-1}·Oe^{-1}·K and $-21.29(5)$ K for $H//ab$, when $C = 0.030280(9)$ emu·g^{-1}·Oe^{-1}·K and $\theta = -24.74(6)$ K for $H//c$. Again, the negative values of θ indicate that the dominant magnetic interaction at high temperature is AFM, which evolves into the long-range AFM ordering below T_N. On the other hand, the corresponding μ_{eff} is 8.255(9) and 8.069(1) μ_{B}/Gd for $H//ab$ and $H//c$, respectively, comparable with those values in $Gd_2CoAl_4Ge_2$ and theoretical value of Gd^{3+} ions. In addition, the nearly perfect overlapping between the ZFC and

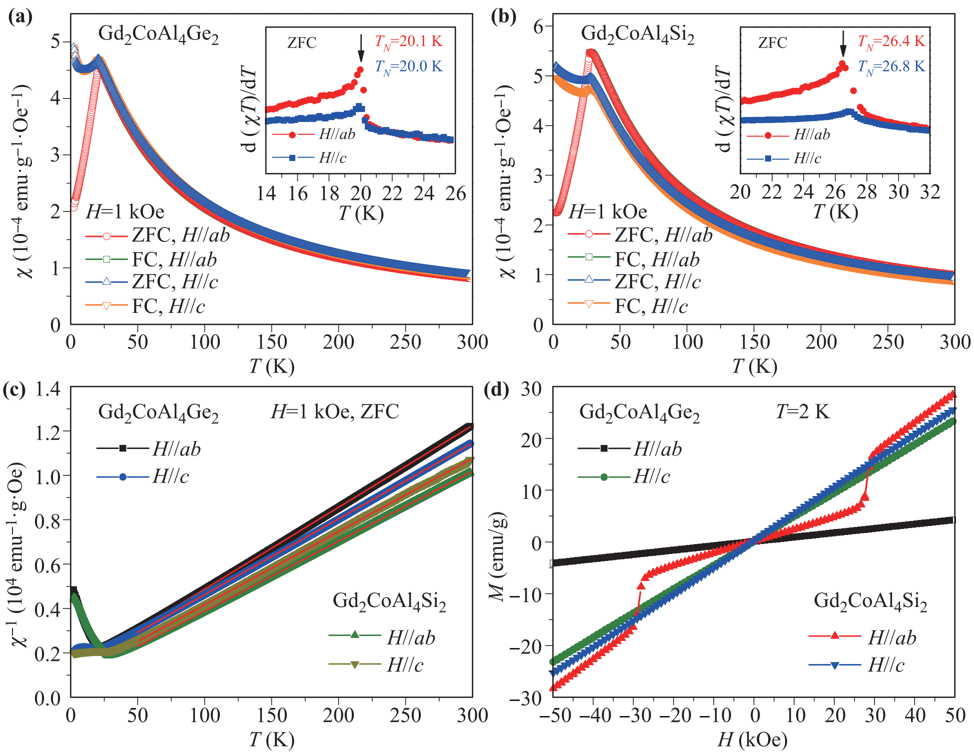

Fig. 3 **(a, b)** Temperature dependence of magnetic susceptibility $\chi(T)$ measured at $H = 1$ kOe for $H//ab$ and $H//c$ with ZFC and FC modes for Gd$_2$CoAl$_4$T$_2$. Insets of (a) and (b): d$(\chi T)/\mathrm{d}T$ vs. T for both field directions with ZFC mode. **(c)** $1/\chi(T)$ as a function of T at $H = 1$ kOe for both field directions with ZFC mode. The solid lines are the linear fits between 50 and 300 K. **(d)** Isothermal magnetization hysteresis loops $M(H)$ for $H//ab$ and $H//c$ at 2 K.

FC $\chi(T)$ curves indicate the absence of magnetic glassy state in these compounds. Figure 3(d) shows the $M(H)$ loops at 2 K for both field directions. For Gd$_2$CoAl$_4$Ge$_2$, the $M(H)$ loops exhibit the linear field dependence without the trend of saturation and hysteresis, irrespective of the field directions. It is consistent with the AFM orders in these materials. For Gd$_2$CoAl$_4$Si$_2$, the $M(H)$ loop also shows similar linear field dependence when $H//c$. Interestingly, the $M(H)$ curve exhibits a sharp jump at $H \sim 29$ kOe when $H//ab$, implying that there is a spin-flop transition, i.e., the spin directions are almost perpendicular to the field direction and nearly antiparallel to each other [12–14].

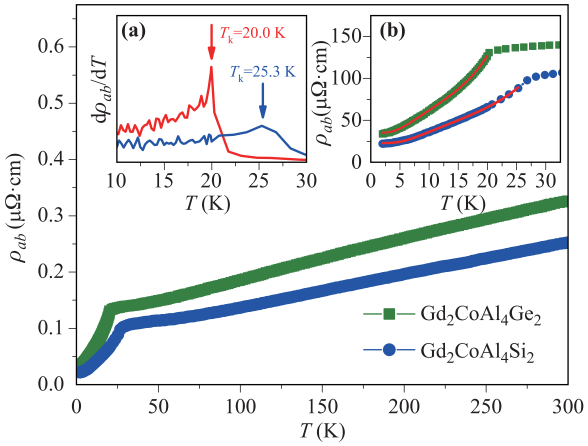

Fig. 4 Temperature dependence of the in-plane resistivity $\rho_{ab}(T)$ of Gd$_2$CoAl$_4$T$_2$ single crystals. Inset: **(a)** dρ_{ab}/dT as a function of T. **(b)** The enlarged part of $\rho_{ab}(T)$ at low-temperature region and the solid lines represent the fits using Eq. (1).

Figure 4 shows the temperature dependence of the in-plane resistivity $\rho_{ab}(T)$ of Gd$_2$CoAl$_4$T$_2$ single crystals. These compounds exhibit metallic behavior in the whole temperatures range. The most notable feature of $\rho_{ab}(T)$ is a sharp drop at low temperature. The determined temperature T_k from the peak of dρ_{ab}/dT curve [Inset (a) of Fig. 4] is 20.0 and 25.3 K for Gd$_2$CoAl$_4$Ge$_2$ and Gd$_2$CoAl$_4$Si$_2$, respectively, consistent with the transition temperature observed in the magnetization and heat capacity data (shown as below). The drop in the $\rho_{ab}(T)$ curve originates from the rapid decrease in the spin disorder scattering below AFM transition. when taking into account the scattering of conduction electrons by phonons and antiferromagnetic magnons, the temperature dependence of $\rho_{ab}(T)$ for $T < T_N$ can be expressed by [15, 16]

$$\rho_{ab}(T) = \rho_0 + AT^5 + B\Delta^2\sqrt{\frac{k_BT}{\Delta}}\,\mathrm{e}^{-\Delta/(k_BT)} \times\left[1+\frac{3\Delta}{2k_BT}+\frac{2}{15}\left(\frac{\Delta}{k_BT}\right)^2\right], \tag{1}$$

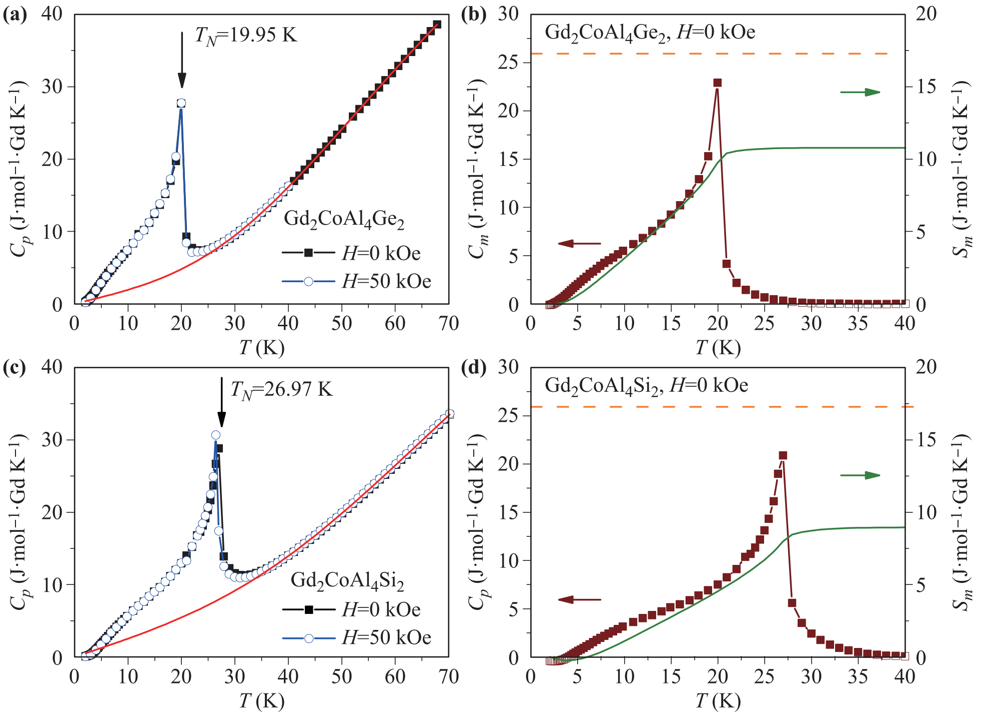

Fig. 5 **(a)** Temperature dependence of heat capacity $C_p(T)$ for $Gd_2CoAl_4Ge_2$ single crystal at $H = 0$ and 50 kOe. The red solid line is a fit by using Eq. (2) at zero field. **(b)** Zero-field magnetic specific heat $C_m(T)$ as a function of T. The right label denotes the calculated magnetic entropy $S_m(T)$. **(c)** $C_p(T)$ vs. T for $Gd_2CoAl_4Si_2$ single crystal at $H = 0$ and 50 kOe. The red solid line is a fit by using Eq. (2) at zero field. **(d)** Temperature dependence of $C_m(T)$ and $S_m(T)$ curves at zero field for $Gd_2CoAl_4Si_2$ single crystal.

where ρ_0 is residual resistivity, A and B is the constants of the electron-phonon and electron-magnon scattering term at low temperature, respectively, k_B is Boltzmann constant, Δ is the magnon gap energy. Both ρ_{ab} curves can be fitted very well [Inset (b) of Fig. 4] and the obtained ρ_0, A, B, and Δ is 35.3(2) μΩ·cm, 0.0107(2) nΩ·cm·K^{-5}, 0.148(2) μΩ·cm·K^{-2}, and 20.2(3) K for $Gd_2CoAl_4Ge_2$, and 22.9(1) μΩ·cm, 0.00211(5) nΩ·cm·K^{-5}, 0.0720(7) μΩ·cm·K^{-2}, and 25.3(3) K for and $Gd_2CoAl_4Si_2$, respectively. The fitted values of Δ are close to their AFM ordering temperature.

Figure 5 shows the temperature dependence of heat capacity $C_p(T)$ for $Gd_2CoAl_4Ge_2$ single crystal. There is a λ-type anomaly with the peak position located at 19.95 K. It is the evidence of bulk long-range AFM ordering and the transition temperature is also consistent with that temperature obtained from $d\chi(T)/dT$ curve [inset of Fig. 3(a)]. Moreover, at $H = 50$ kOe the $C_p(T)$ curve is perfectly overlapped with that at zero field, indicating that that the field of 50 kOe has a negligible influence on the AFM transition of $Gd_2CoAl_4Ge_2$. Assuming that the total heat capacity consists of electronic (C_e), lattice (C_{ph}) and magnetic (C_m) components, C_m can be estimated by the subtraction of C_e and C_{ph}. Because the absence of non-magnetic counterpart of this material, we fitted the heat capacity data in the high-temperature range ($T \geq 35$ K) well away from T_N when only considering C_e and C_{ph} and then extrapolated to 2 K. Using the Debye function, it has

$$\begin{aligned} C_p(T) &= C_e + C_{ph} \\ &= \gamma T + 9RC\left(\frac{T}{\Theta_D}\right)^3 \int_0^{\Theta_D/T} \frac{x^4 e^x}{(e^x-1)^2} dx, \qquad (2) \end{aligned}$$

where γ is the Sommerfeld coefficient, R is the gas constant ($R = 8.314$ J·mol^{-1}·K^{-1}), Θ_D is Debye temperature, C is a fitting parameter. The fitted γ and Θ_D is 355(2) J·mol^{-1}·Gd K^{-2} and 321.9(6) K, respectively. The fitted curve is shown in Fig. 5(a) (red solid line) and after subtracting the electronic and lattice contributions from $C_p(T)$, we obtain the $C_m(T)$ curve [Fig. 5(b)]. Then, the magnetic entropy $S_m(T)$ can be calculated using the integral $S_m(T) = \int_0^T C_m/T dT$. As shown in Fig. 5(b), the $S_m(T)$ increases gradually when increasing temperature and then tends to saturate above T_N. The obtained S_m up to 40 K is about 10.8 J·mol^{-1}·Gd K^{-1}, which is about 62% of theoretical value [$R\ln(2J + 1) =$ 17.3 J·mol^{-1}·Gd K^{-1} for Gd^{3+} ions with $J = 7/2$]. This discrepancy may originate from an overestimation of the electronic and lattice contributions which may cause a reduction in $S_m(T)$. Similar to $Gd_2CoAl_4Ge_2$, there is also a peak at 26.97 K for $Gd_2CoAl_4Si_2$ at zero field [Fig. 4(c)], consistent with the results of magnetization measurement. In contrast to $Gd_2CoAl_4Ge_2$, at high field ($H = 50$ kOe), the peak of $C_p(T)$ shifts to lower temperature slightly

($T_N = 26.45$ K), implying the suppression of AFM order by field. This could be related to the metamagnetic transition in $Gd_2CoAl_4Si_2$. After subtracting the electronic and lattice contributions from $C_p(T)$, the obtained $C_m(T)$ is shown in Fig. 4(d) and it exhibits similar behavior as in $Gd_2CoAl_4Ge_2$. The estimated S_m up to 40 K is 8.9 $\mathrm{J \cdot mol^{-1} \cdot Gd\ K^{-1}}$, which is about 51% of theoretical value for Gd^{3+} ions. Again, this discrepancy may also be due to the overestimation of the C_e and C_{ph}.

4 Conclusion

In summary, we report the physical properties of two new quaternary compounds $Gd_2CoAl_4T_2$ (T = Si, Ge) single crystals grown by using Al flux. $Gd_2CoAl_4T_2$ belong to the tetragonal space group I4/mmm and the fitted a- and c-axial lattice parameters are 4.1392(3) Å and 19.543(2) Å for $Gd_2CoAl_4Ge_2$ and 4.1099(1) Å and 19.4146(8) Å for $Gd_2CoAl_4Si_2$. The crystal structure consists of layers of $CoAl_4T_2$ slab separated by bilayers Gd atoms. Both compounds are AFM metals and the T_N is about 20 and 27 K for $Gd_2CoAl_4Ge_2$ and $Gd_2CoAl_4Si_2$, respectively. Heat capacity measurements confirm the bulk feature of these AFM transitions. The long-range antiferromagnetism in these materials may solely originate from the magnetic interaction between Gd^{3+} ions and the Co ions should have negligible local moments. Moreover, the $Gd_2CoAl_4Ge_2$ exhibits metamagnetic transition when the field is along the ab plane and larger than 29 kOe.

Acknowledgements This work was supported by the National Natural Science Foundation of China (Grant Nos. 11574394, 11774423, 11822412, and 51608273), the Fundamental Research Funds for the Central Universities (Grant No. 2017RC20), the Natural Science Foundation of the Jiangsu Higher Education Institutions of China (No. 16KJB560008), the Young Researcher Program Nanjing Forestry University of China (No. CX2016023), Key Laboratory of Advanced Building Materials of Anhui Province of China (No. JZCL201603KF), and State Key Laboratory of High Performance Civil Engineering Materials of China (No. 2016CEM004).

References

1. P. C. Canfield and Z. Fisk, Growth of single crystals from metallic fluxes, *Philos. Mag. B* 65, 1117 (1992)
2. M. G. Kanatzidis, R. Pöttgen, and W. Jeitschko, The metal flux: A preparative tool for the exploration of intermetallic compounds, *Angew. Chem. Int. Ed.* 44(43), 6996 (2005)
3. S. Okada, Y. Yu, T. Lundström, K. Kudou, and T. Tanaka, Crystal growth and some properties of LuB_4, $LuAlB_4$, and Lu_2AlB_6, *Jpn. J. Appl. Phys.* 35(Part 1, No. 9A), 4718 (1996)
4. S. Okada, K. Kudou, K. Iizumi, K. Kudaka, I. Higashi, and T. Lundström, Single-crystal growth and properties of CrB, Cr_3B_4, Cr_2B_3 and CrB_2 from high-temperature aluminum solutions, *J. Cryst. Growth* 166(1–4), 429 (1996)
5. B. Sieve, X. Z. Chen, J. A. Cowen, P. Larson, S. D. Mahanti, and M. G. Kanatzidis, Multinary intermetallics from molten Al. Synthesis of $SmNiAl_4Ge_2$ and $YNiAl_4Ge_2$. Possible spin frustration in separated triangular Sm^{3+} layers, *Chem. Mater.* 11(9), 2451 (1999)
6. X. Z. Chen, S. Sportouch, B. Sieve, P. Brazis, C. R. Kannewurf, J. A. Cowen, R. Patschke, and M. G. Kanatzidis, Exploratory synthesis with molten aluminum as a solvent and routes to multinary aluminum silicides. $Sm_2Ni(Ni_xSi_{1-x})Al_4Si_6$ ($x = 0.18 - 0.27$): A new silicide with a ferromagnetic transition at 17.5 K, *Chem. Mater.* 10(10), 3202 (1998)
7. B. Sieve, X. Z. Chen, R. Henning, P. Brazis, C. R. Kannewurf, J. A. Schultz, and M. G. Kanatzidis, Cubic aluminum silicides $RE_8Ru_{12}Al_{49}Si_9$ (Al_xSi_{12-x}) (RE = Pr, Sm) from liquid aluminum. Empty $(Si,Al)_{12}$ cuboctahedral clusters and assignment of the Al/Si distribution with neutron diffraction, *J. Am. Chem. Soc.* 123(29), 7040 (2001)
8. B. Sieve, P. N. Trikalitis, and M. G. Kanatzidis, Quaternary germanides formed in molten aluminum: $Tb_2NiAl_4Ge_2$ and $Ce_2NiAl_{6-x}Ge_{4-y}$ ($x \sim 0.24$, $y \sim 1.34$), *Z. Anorg. Allg. Chem.* 628(7), 1568 (2002)
9. G. Demchenko, J. Kónczyk, P. Demchenko, R. Gladyshevskii, W. Majzner, and L. Muratova, Quaternary alumogermanides in the Er-{Co,Ni}-Al-Ge systems, *Chem. Met. Alloys* 1, 254 (2008)
10. M. E. Fisher, Relation between the specific heat and susceptibility of an antiferromagnet, *Philos. Mag.* 7(82), 1731 (1962)
11. F. Canepa, M. Napoletano, M. L. Fornasini, and F. Merlo, Structure and magnetism of Gd_2Co_2Ga, Gd_2Co_2Al and $Gd_{14}Co_3In_{2.7}$, *J. Alloys Compd.* 345(1–2), 42 (2002)
12. F. B. Anderson and H. B. Callen, Statistical mechanics and field-induced phase transitions of the Heisenberg antiferromagnet, *Phys. Rev.* 136(4A), A1068 (1964)
13. Y. Shapira and S. Foner, Magnetic phase diagram of MnF_2 from ultrasonic and differential magnetization measurements, *Phys. Rev. B* 1(7), 3083 (1970)
14. F. Keffer and H. Chow, Dynamics of the antiferromagnetic spin-flop transition, *Phys. Rev. Lett.* 31(17), 1061 (1973)
15. S. N. de Medeiros, M. A. Continentino, M. T. D. Orlando, M. B. Fontes, E. M. Baggio-Saitovitch, A. Rosch, and A. Eichler, Quantum critical point in $CeCo(Ge_{1-x}Si_x)_3$, *Physica B* 281–282, 340 (2000)
16. M. B. Fontes, J. C. Trochez, B. Giordanengo, S. L. Budko, D. R. Sanchez, E. M. Baggio-Saitovitch, and M. A. Continentino, Electron-magnon interaction in RNiBC (R = Er, Ho, Dy, Tb, and Gd) series of compounds based on magnetoresistance measurements, *Phys. Rev. B* 60(9), 6781 (1999)